

Analytical results on the role of flexibility in flapping propulsion

M. Nicholas J. Moore †

Courant Institute of Mathematical Sciences, New York University, NY 10012, USA
Department of Mathematics and Geophysical Fluid Dynamics Institute, Florida State
University, FL 32306, USA

(Received 24 August 2014)

Wing or fin flexibility can dramatically affect the performance of flying and swimming animals. Both laboratory experiments and numerical simulations have been used to study these effects, but analytical results are notably lacking. Here, we develop small-amplitude theory to model a flapping wing that pitches passively due to a combination of wing compliance, inertia, and fluid forces. Remarkably, we obtain a class of exact solutions describing the wing's emergent pitching motions, along with expressions for how thrust and efficiency are modified by compliance. The solutions recover a range of realistic behaviors and shed new light on how flexibility can aid performance, the importance of resonance, and the separate roles played by wing and fluid inertia. The simple, robust estimates afforded by our theory will likely be valuable even in situations where details of the flapping motion and wing geometry differ.

1. Introduction

For flying and swimming animals alike, the flapping of wings or fins is a ubiquitous form of locomotion. Unlike traditional man-made wings, biological wings or fins are subject to large elastic deformations, which can lead to greatly improved propulsive performance (see Fish 1993; Vogel 1994; Young *et al.* 2009; Wu 2011; Lucas *et al.* 2014). In fact, it is widely believed that wing-flexibility will be exploited in next generation air-and-water-based technologies, such as micro-air vehicles (see Rozhdestvensky & Ryzhov 2003; Shang *et al.* 2009; Ristroph & Childress 2014).

Owing to such applications as well as to our own natural curiosity, there has been a developing interest to understand how wing flexibility alters propulsion. Laboratory experiments of wings flapping against imposed flows (see Heathcote & Gursul 2007; Dewey *et al.* 2013) or locomoting freely (see Vandenberghe *et al.* 2006; Spagnolie *et al.* 2010; Thiria & Godoy-Diana 2010) have provided a rich foundation of observations. Meanwhile, numerical simulations based on vortex-shedding models (see Katz & Weihs 1978; Alben 2008; Michelin & Smith 2009; Alben *et al.* 2012) or direct Navier-Stokes and Boltzmann solvers (see Spagnolie *et al.* 2010; Masoud & Alexeev 2010; Kang *et al.* 2011; Dai *et al.* 2012) have advanced our understanding of the principles at play.

These studies vary in the types of kinematics and flexibility used. Most often the flexibility is either uniform along the wing or localized by a torsional spring, and the driving is either a pitching or a heaving motion. Despite these differences, the studies all reveal that wing compliance can lead to substantial improvements in performance, as measured by the thrust the wing generates, its propulsive efficiency, or its free-swimming speed. Further, performance can degrade if the driving frequency is sufficiently high, pointing

† Email addresses for correspondence: moore@math.fsu.edu, nickmoore83@gmail.com

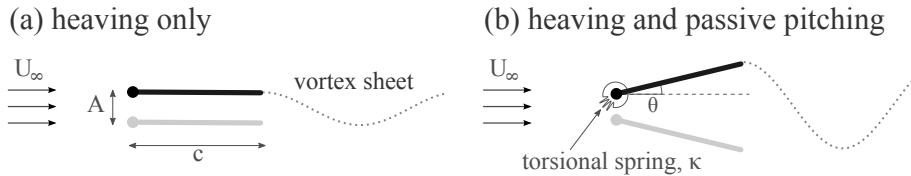


FIGURE 1. Schematic and notation. (a) As a rigid wing heaves in a flow it sheds a vortex-sheet wake. (b) A torsional spring located at the leading-edge allows the wing to pitch passively.

to a frequency of optimal performance. Several recent studies have found this optimal frequency to be comparable to a natural resonance of the wing-fluid system, albeit with a fair amount of variation in the reported ratio (see Michelin & Smith 2009; Masoud & Alexeev 2010; Thiria & Godoy-Diana 2010; Kang *et al.* 2011; Ramananarivo *et al.* 2011; Alben *et al.* 2012). Recently, Dewey *et al.* (2013) used scaling arguments to estimate the optimal driving frequency and thrust, which gave good collapse of their experimental data. For a self-propelled wing, Spagnolie *et al.* (2010) found that increasing the driving beyond the optimal frequency first slows the wing’s motion, and, if the frequency is high enough, can even reverse the natural swimming direction. These studies illustrate just some of the rich behavior that can arise from the interplay between a fluid and flexible propulsor, and despite recent progress, a complete understanding of the underlying principles is lacking. In particular, analytical results that capture some of the system’s essential behavior have proven elusive, and this is the purpose of the present study.

In this paper, we consider a so-called torsional flexibility model, in which a rigid wing is affixed to a torsional spring at its leading edge. When flapped in a fluid, the wing can deflect angularly, or pitch, in response to the forces acting on it. We choose this model primarily for its simplicity, although it is a situation that can also be found in nature, for example the pitching motions of insect wings that occur due to joint flexibility (see Ennos 1988; Bergou *et al.* 2007). To determine the fluid flow, we perform asymptotic analysis in the limit of small driving amplitude, as was originally introduced by Wu (1961) for *prescribed* kinematics. Extending Wu’s analysis, we couple this flow to the initially unknown wing kinematics through a torque balance. Remarkably, this yields a class of exact solutions describing the emergent pitching motions, along with expressions for the thrust generated by the wing and the power required to drive it. The solutions recover a range of realistic behaviors, including a resonant mode that produces optimal thrust and a high-frequency mode in which performance degrades. Our results even compare well to previous experiments once we take into account an additional drag term. Overall, these small-amplitude calculations illustrate how flexibility can aid propulsion, the importance of resonance, and the separate roles played by wing and fluid inertia.

2. Exact solutions

As diagrammed in Fig. 1, we consider a thin wing of chord c , driven at its leading-edge by a periodic heaving motion of amplitude A and frequency f , and held against an oncoming flow of speed U_∞ . A torsional spring of stiffness κ at the leading edge allows the wing to pitch passively, and we treat the fluid as inviscid except for a vortex sheet shed from the trailing edge. In the following, we solve for the emergent wing kinematics as they are coupled to the surrounding fluid flow. Our calculations use the small-amplitude limit of $A/c \ll 1$ and $fA/U_\infty \ll 1$ (small Strouhal number), though no restriction will be placed on the ratio fc/U_∞ , which will allow different temporal modes to emerge.

2.1. Fluid flow for given kinematics

We first consider the fluid flow arising from prescribed heaving and pitching wing kinematics. To nondimensionalize, we scale length on $c/2$, time on $1/f$, and velocity on $cf/2$. We introduce the dimensionless free-stream velocity $U = 2U_\infty/(cf)$, and consider the flow field relative to this value, $\mathbf{u} = (U + u, v)$. Using the small-amplitude assumption, we linearize the incompressible Euler equations to obtain

$$(\partial_t + U\partial_x)\mathbf{u} = \nabla\varphi, \quad (2.1)$$

$$\nabla \cdot \mathbf{u} = 0. \quad (2.2)$$

Here, $\varphi = 4(p_\infty - p)/(\rho c^2 f^2)$ is a normalized pressure, also called the Prandtl acceleration potential (Wu 1961). We consider time-harmonic heaving and pitching kinematics, represented by the wing's vertical displacement $h \ll 1$ as

$$h(x, t) = (\beta_0/2 + \beta_1 x) e^{2\pi j t} \quad \text{for } -1 \leq x \leq 1. \quad (2.3)$$

Here, the leading edge of the wing is located at $x = -1$ and the trailing edge at $x = 1$, while β_0 and β_1 are parameters for the motion and j is the imaginary unit. Hereafter, it is implicit that the real part in j should be taken. The fluid flow must be tangential to the wing surface, which upon linearization, gives the boundary conditions

$$(\partial_t + U\partial_x)h = v \quad \text{as } y \rightarrow \pm 0, \quad -1 \leq x \leq 1. \quad (2.4)$$

Meanwhile, the Kutta condition requires u and v to be finite at the trailing edge ($x = 1$), thus dictating the amount of vorticity shed there.

Following Wu (1961), we exploit properties of the normalized pressure, φ , to solve Eqs. (2.1)–(2.4) in the small-amplitude limit, $\beta_0, \beta_1 \ll 1$. The advantage of this approach is that pressure is continuous throughout the fluid, unlike velocity which suffers a discontinuity across the trailing vortex sheet. Taking the divergence of Eq. (2.1) and using incompressibility shows that φ is a harmonic function. We identify physical space with the complex plane $z = x + iy$, and introduce the complex velocity $w = u - iv$. Since φ is harmonic, it is the real part of an analytic function $g(z, t) = \varphi + i\psi$. To determine g we conformally map the fluid domain to the exterior of the unit circle via $z = (\zeta + 1/\zeta)/2$. The details of the calculation can be found in Wu (1961), which we also summarize in Appendix A. The resulting expression for g is

$$g(z, t) = i \left(a_0(\zeta + 1)^{-1} + \sum_{n=1}^{\infty} a_n \zeta^{-n} \right) e^{2\pi j t}, \quad (2.5)$$

$$a_0 = -2\pi j U C(\sigma) \beta_0 + 2\pi j U (1 - C(\sigma)) \beta_1 - 2U^2 C(\sigma) \beta_1, \quad (2.6)$$

$$a_1 = 2\pi^2 \beta_0 - 4\pi j U \beta_1, \quad a_2 = \pi^2 \beta_1, \quad a_n = 0 \quad \text{for } n > 2. \quad (2.7)$$

Here, we have introduced the reduced frequency $\sigma = \pi f c / U_\infty$ and the Theodorsen function $C(\sigma) = K_1(j\sigma)/(K_0(j\sigma) + K_1(j\sigma))$, where K_0 and K_1 are modified Bessel functions of the second kind. For given kinematics, Eqs. (2.5)–(2.7) completely determine the flow field around the wing, and our next task is to couple this flow to the wing's torque balance. Note that $\sigma = 2\pi/U$, and so this solution depends on a single dimensionless parameter which can be taken to be either U or σ .

2.2. Coupling the kinematics and flow

To determine the wing kinematics, we first set the heaving amplitude of the leading edge ($x = -1$) to the dimensionless value $\varepsilon = A/c$. Using Eq. (2.3), this gives the constraint

$$\beta_0/2 - \beta_1 = \varepsilon. \quad (2.8)$$

Without loss of generality, we have assumed Eq. (2.3) to be real valued at $t = 0$, i.e. we have set an initial time. Next, we consider the torques that act on a passively pitching wing as in Fig. 1(b). For a wing of density ρ_s (mass per unit area) and infinitesimal thickness b , the moment of inertia about the leading edge is $I = \rho_s b c^3 / 3$. The pitching angle $\theta(t)$ then satisfies

$$I\ddot{\theta} = -\kappa\theta + N_f + N_i. \quad (2.9)$$

Here, N_f is the torque the fluid exerts on the wing and N_i is an inertial torque resulting from the vertical acceleration of the leading edge, i.e. the pitching point, during flapping. Using the same scales as before, the dimensionless form of this equation is

$$\frac{16}{3}R\ddot{\theta} = -4KU^2\theta + \tilde{N}_f + \tilde{N}_i, \quad (2.10)$$

$$R = \frac{b\rho_s}{c\rho}, \quad K = \frac{\kappa}{\rho U_\infty^2 c^2}, \quad (2.11)$$

where tildes indicate dimensionless variables, and we have introduced the new parameters R and K : R measures the ratio of wing to fluid inertia and K measures the spring stiffness as compared to fluid forces. Although we have assumed the wing is thin, $b \ll c$, it may be composed of heavy material, $\rho_s \gg \rho$, and so we do not necessarily assume that R is small.

The quantity \tilde{N}_i depends only on the driving motion, but to determine \tilde{N}_f the kinematics must be coupled to the flow described by Eqs. (2.5)–(2.7) (see Appendix A). The resulting expressions are

$$\tilde{N}_i = 8\pi^2 R(\beta_0 - 2\beta_1)e^{2\pi jt} \quad (2.12)$$

$$\tilde{N}_f = \frac{\pi}{2}(a_0 + 2a_1 + a_2)e^{2\pi jt}. \quad (2.13)$$

With these terms known, we consider Eq. (2.10) with time-harmonic pitching $\theta = \theta_0 e^{2\pi jt}$. Using the small-amplitude assumption in Eq. (2.3) gives $\theta_0 \sim \beta_1$, which reduces Eq. (2.10) to a linear, algebraic equation, $D_0\beta_0 + D_1\beta_1 = 0$, with coefficients

$$D_0 = 48R + 12\pi - 6jUC, \quad (2.14)$$

$$D_1 = 32R + 3\pi - 24KU^2/\pi^2 - 18jU - 6jUC - 6U^2C/\pi. \quad (2.15)$$

Combining this with Eq. (2.8) gives the following exact solutions for the wing kinematics,

$$\beta_0 = \frac{2\varepsilon D_1}{2D_0 + D_1}, \quad \beta_1 = \frac{-2\varepsilon D_0}{2D_0 + D_1}. \quad (2.16)$$

We illustrate the motion described by these solutions in Fig. 2, where we show a wing of mass ratio $R = 0$ and stiffness $K = 4$ driven at three different frequencies. When driven at the lowest frequency $\sigma = 1$, the wing primarily heaves as it translates through the fluid, with only slight pitching (Fig. 2(a)). Increasing the driving frequency to $\sigma = 2$ creates a much more pronounced pitching motion that lags the driving by a quarter phase (Fig. 2(b)). The combination of fluid inertia and elasticity seems to ‘fling’ the trailing edge of the wing. As we will see later, this particular motion results from driving near the system’s resonant frequency, and it will have important implications for the wing’s performance. Increasing the frequency yet higher to $\sigma = 10$ causes the pitching to become out of phase with the driving (Fig. 2(c)) as inertial effects seem to dominate.

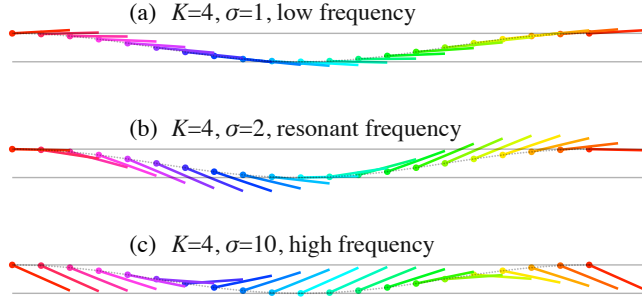


FIGURE 2. Visualizing the emergent kinematics given by Eq. (2.16). A single wing ($R = 0$, $K = 4$) is driven at three different frequencies. (a) A low driving frequency produces only slight pitching motions. (b) When driven near resonance, the pitching is much more pronounced. (c) Driving the wing at high frequency results in out-of-phase pitching.

3. Results

How do the emergent pitching motions affect propulsion? With both the kinematics and fluid flow determined, we calculate in Appendix B the forward thrust generated by the wing and the power required to drive it. In this section, we present results in terms of coefficients of thrust and power,

$$C_T = \frac{\bar{T}}{\frac{1}{2}\pi^3\rho f^2 A^2 c}, \quad (3.1)$$

$$C_P = \frac{\bar{P}}{\frac{1}{2}\pi^3\rho U_\infty f^2 A^2 c}. \quad (3.2)$$

Here, \bar{T} and \bar{P} are the dimensional thrust and power, each averaged over one flapping period (indicated by the overbar). The thrust includes a contribution from the pressure difference across the wing, as well as a leading-edge suction term that results from the singular flow near $z = -1$. The power is the work per unit time needed to drive the wing. Importantly, we have scaled both thrust and power on A^2 , which make C_T and C_P independent of ε . That is, our results are independent of the driving amplitude, as long as it is sufficiently small.

In what follows, we will assess the effects of wing compliance by comparing a pitching wing to one that is clamped at its leading edge. In particular, we will examine the driving frequencies that lead to optimal performance and the kinematics associated with this regime. Our primary performance metric is the forward thrust, though one might also be interested in the thrust produced for a given input power, and so we introduce the so-called propulsive efficiency $\eta = C_T/C_P$.

3.1. Performance

We first consider massless wings, $R = 0$, so that the only source of inertia is the fluid. This limit describes, for example, the fins of many swimming animals since such fins are typically thin and of a density similar to water. In Fig. 3(a), we show how the thrust coefficient varies with driving frequency for several wings having different spring stiffnesses, K . First, $K = \infty$ (black curve) corresponds to a clamped wing that cannot pitch, and this serves as our control. For this wing, C_T tends to a constant for both $\sigma \rightarrow 0$ and $\sigma \rightarrow \infty$, meaning that the raw thrust scales like f^2 as it vanishes at low frequencies and grows at high frequencies. Next, $K = 0$ (yellow curve) corresponds to a hinged wing

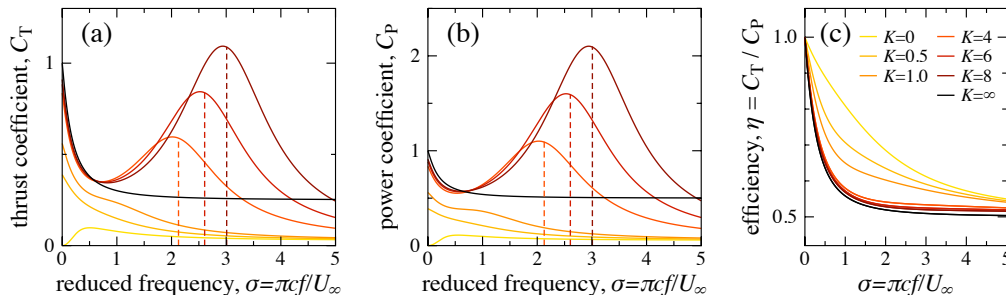


FIGURE 3. Propulsive performance of pitching wings. (a) Thrust coefficient versus reduced driving frequency for different wings. The black curve, $K = \infty$, represents a clamped wing, while the others have finite stiffnesses. The yellow curves, $K = 0, 0.5, 1$, are the most compliant and the red curves, $K = 4, 6, 8$, are the stiffest. All wings are massless, $R = 0$. The stiff wings produce optimal thrust at a frequency well predicted by Eq. (3.4) (dashed vertical lines). (b) Input-power coefficient and (c) propulsive efficiency for the same set of wings.

that can pitch freely. This wing produces significantly less thrust than the clamped wing, as do those with relatively compliant springs ($K = 0.5, 1$).

The most interesting cases are when the spring stiffness is larger, e.g. $K = 4, 6, 8$, shown by the red curves in Fig. 3(a). For these wings, the thrust coefficient agrees closely with the clamped-wing value at low frequencies, increases and obtains a maximum, and then falls off below the clamped-wing value at higher frequencies. Thus, a small amount of compliance leads to thrust *enhancement* at moderate frequencies and thrust *reduction* at higher frequencies. This finding is consistent with several previous studies (see Heathcote & Gursul 2007; Alben 2008; Spagnolie *et al.* 2010; Dewey *et al.* 2013), even those in which the setup is somewhat different, for example, the entire wing surface is flexible. In our setup the thrust enhancement can be quite considerable. Figure 3(a) shows that a wing with $K = 8$ produces up to three times the thrust of a clamped wing. Furthermore, the trend of the three red curves indicates that stiffer springs yield higher peak thrusts, but require higher driving frequencies to achieve their peak.

In Fig. 3(b), we show the coefficient of power required to drive the wings. In the clamped case, C_P tends to a constant at high driving frequencies, indicating we have chosen a sensible nondimensionalization. Meanwhile, the power required to heave the most compliant wings (yellow curves) is generally much smaller. This agrees with the intuition that a hinged wing can feather, i.e. align with the instantaneous flow direction, and thus requires little input power. Once again, the most interesting cases are larger K , shown by red curves. Here, the power coefficient follows a trend similar to thrust, peaking at an intermediate driving frequency and falling off below the clamped-wing value at higher frequencies. In Fig. 3(c), we show how the propulsive efficiency $\eta = C_T / C_P$ varies with driving frequency for each of these wings. Generally, efficiency decreases with driving frequency, and the most compliant wings show the greatest efficiencies. Interestingly, none of the wings exhibit an optimum with respect to η , even the stiff wings (red curves) for which the peaks in thrust and power offset one another.

3.2. Kinematics

We now relate these performance characteristics back to the wing kinematics. First, reconciling the motion illustrated in Fig. 2 with the curves for $K = 4$ in Fig. 3, it appears that thrust (and power) are strongly influenced by the kinematics, particularly by the amplitude of the trailing-edge motion. At low frequencies, the wing kinematics are affected little by elasticity (Fig. 2(a)), and, consequently, the performance is nearly the

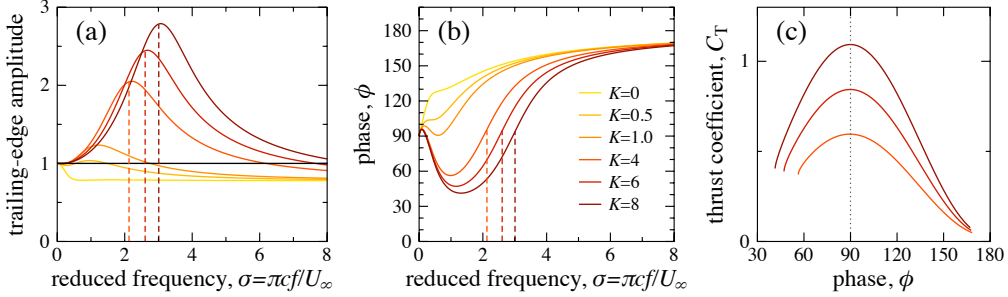


FIGURE 4. Quantifying the kinematics. (a) Trailing-edge amplitude versus reduced frequency for the same wings considered earlier: $K = 0, 0.5, 1$ (yellow), $K = 4, 6, 8$ (red) and $K = \infty$ (black). For the stiff wings, the trailing-edge amplitude obtains a maximum at the resonant frequency σ_r from Eq. (3.4) (dashed vertical lines). (b) Phase difference ϕ between pitching and driving for the same set of wings. When driven at resonance, each of the stiff wings shows a phase difference of $\phi = 90^\circ$. (c) Thrust coefficient versus phase difference for the stiff cases. Indeed, each wing produces peak thrust when $\phi = 90^\circ$.

same as the clamped case. At a driving frequency of $\sigma = 2$, the emergent pitching motion allows the trailing edge to reach larger amplitude (Fig. 2(b)), and this coincides with the peak thrust production seen in Fig. 3(a). At higher frequencies, the out-of-phase pitching reduces the trailing-edge amplitude (Fig. 2(c)) and the wing produces significantly less thrust.

To quantify this relationship further, we use Eq. (2.16) to calculate the trailing-edge amplitude (scaled on the driving amplitude) as

$$h_1 = \frac{D_1 - 2D_0}{D_1 + 2D_0}. \quad (3.3)$$

In Fig. 4(a), we show how h_1 varies with driving frequency for the seven wings considered in Section 3.1. In the stiff cases, h_1 exhibits a peak at nearly the same driving frequency as does C_T and C_P . Importantly, this gives us a way to determine the frequency of peak thrust production, as the above expression for h_1 is more manageable to optimize than C_T . In the stiff-spring limit, we calculate the so-called *resonant* frequency σ_r that maximizes h_1 as

$$\sigma_r \sim \sqrt{\frac{96K}{128R + 27\pi}} \quad \text{for } K \gg 1. \quad (3.4)$$

For $K = 4, 6, 8$, we indicate this approximate σ_r by the dashed vertical lines in Fig. 4(a), showing close agreement with the true h_1 -peaks. Further, we show the same three values of σ_r on the plots of C_T and C_P (Figs. 3(a) and (b)), demonstrating that this frequency produces near optimal thrust and power coefficients.

The wing kinematics are not only characterized by the trailing-edge amplitude, but also by the phase difference ϕ between pitching and driving. In Fig. 4(b), we show how ϕ varies with driving frequency for the same wings considered earlier. For the stiff cases (red curves), the phase difference is nearly 90 degrees when driven at resonance, corresponding to the flinging kinematics from Fig. 2(b). As the driving frequency increases further, ϕ approaches 180 degrees, which corresponds to the out-of-phase kinematics from Fig. 2(c). In Fig. 4(c) we show the thrust coefficient against ϕ for the three stiff wings, $K = 4, 6, 8$, confirming that peak performance is indeed associated with $\phi = 90^\circ$ in each case. Interestingly, many swimming animals operate with a phase difference near 90° when flapping (see Rozhdestvensky & Ryzhov 2003). While other studies suggest this mode

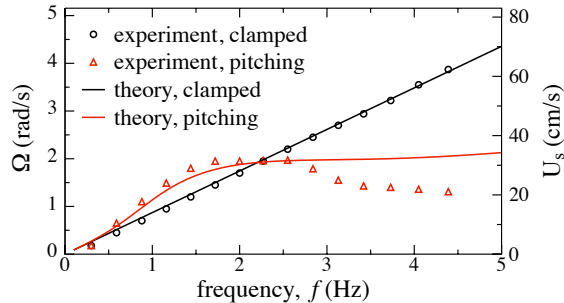


FIGURE 5. Comparison to the experiments of Spagnolie *et al.* (2010). The measured angular velocity Ω of a clamped wing (black circles) and a pitching wing (red triangles) plotted against driving frequency, with the equivalent linear swimming speed U_s on the right axis. The solid curves show the speeds predicted by our small-amplitude theory for the same two wings (black and red respectively). For the pitching wing, the theory captures the overall trend of the data and even shows quantitative agreement at low frequencies.

is preferred because it produces optimal efficiency (see Heathcote & Gursul 2007), our results suggest it yields optimal thrust.

4. Comparison to previous experiments

To assess how well our small-amplitude theory models real flapping propulsion we briefly compare to some previous experimental results. We focus on the experiments of Spagnolie *et al.* (2010), whose torsional-flexibility setup is most similar to ours. In those experiments, a wing was driven by a periodic heaving motion and allowed to rotate freely about a vertical shaft, making circular orbits within a water tank. The wing's rotation represents free swimming and avoids the difficulties of infinite travel distance associated with rectilinear translation. In the experiments, the wing (chord 8 cm and span 13 cm) was driven with an amplitude of 2.7 cm (peak to peak), and was either clamped at its leading edge or furnished with a torsional spring ($\kappa^* = 0.15$ Nm/rad) to allow passive pitching, just as in our setup. Figure 5 shows measurements of the angular velocity Ω as it varies with the driving frequency f for both wings. Evidently, flexibility improves performance at low driving frequencies and hinders it at higher frequencies, in qualitative agreement with our finding from Section 3. To relate the measurements to our 2D theory, we calculate an equivalent linear swimming speed $U_s = \Omega d$, where $d = 16.5$ cm is the distance from the axle to the wing's midpoint (along the span), and we show U_s on the right axis of Fig. 5.

To draw a quantitative comparison, we would like to use the small-amplitude solutions to determine U_s , but an immediate difficulty arises: the thrust shown in Fig. 3(a) is positive for all driving frequencies, meaning that a self-propelled wing would accelerate indefinitely. This behavior is simply due to the lack of drag in our inviscid model. An experiment can only be performed at finite Reynolds number and with wings of finite thickness, introducing both viscous and form drag. In Spagnolie *et al.* (2010), the linear trend of the clamped-wing measurements from Fig. 5 suggests that for thrust to scale as f^2 , drag must scale as $\Omega^2 \propto U_s^2$, indicating that form drag dominates[†]. We therefore include in our calculations a time-averaged drag term $\overline{D} = -(C_D/2)\rho U_s^2 c$ and calculate U_s as the speed at which thrust and drag balance, $\overline{T} + \overline{D} = 0$.

[†] Despite the high Reynolds number, it is not obvious a priori that form drag should dominate since the wing is thin (i.e. streamlined).

Although the drag coefficient, C_D , in reality depends on the details of the kinematics, here we seek a straightforward assessment of how well the small-amplitude theory captures effects of compliance, and so we will keep C_D constant throughout. First, by fitting the clamped-wing data from Fig. 5, we find $C_D = 0.3$, which is a reasonable value for a thin wing having a moderate (time-averaged) angle of attack to its swimming direction. We then calculate the swimming speed of a pitching wing having the same spring constant used in Spagnolie *et al.* (2010). Shown by the red curve in Fig. 5, the calculated U_s captures the overall trend of the experimental data and even shows quantitative agreement at low driving frequencies. The theory does a remarkable job at capturing two important frequencies: the ‘optimal’ frequency, where the pitching wing outperforms the clamped wing by the widest margin, and the ‘break-even’ frequency, where the two wings have the same swimming speed. The theory also demonstrates underperformance of the pitching wing at high frequencies, although the agreement with measurements is not as close in this regime. The discrepancy is likely due to finite-amplitude effects, for example leading-edge vortex shedding, which may be present in the experiments since $A/c = 0.34$. We note that some of these effects may be crudely accounted for by our additional drag term, but not their dependence on driving frequency since we kept C_D constant.

In the experiments of Spagnolie *et al.* (2010), the wing most often propelled with the torsional spring leading its motion. This direction defines positive Ω , and it has been an implicit assumption in our theory. However, at sufficiently high driving frequencies, Spagnolie *et al.* (2010) observed that the wing could reverse its natural swimming direction and achieve a so-called ‘retrograde motion’ (data not shown in Fig. 5). It would be an interesting extension of our theory to instead locate the torsional spring at the wing’s *trailing* edge to determine if negative U_s is possible as a steady state. While we leave this for future work, the results in the next section provide some preliminary insight into the retrograde effect.

5. Effects of wing inertia

We now shift the focus back to our small-amplitude theory and ask how propulsive performance changes when the wing itself has inertia. This is an important consideration for the flight of insects and birds, where the wings are thin and much denser than air so that the wing/fluid inertia ratio can be order one or larger (see Bergou *et al.* 2007; Dai *et al.* 2012). We show in Fig. 6 the thrust coefficient against driving frequency for the same K -values considered in Section 3, but now with an inertia ratio of $R = 1$. For the stiff springs (red curves), wing inertia does not alter the qualitative trend of C_T , although the peak-thrust values are somewhat larger and occur at lower driving frequencies. The compliant wings, however, actually produce negative thrust for certain driving frequencies, which was not observed when $R = 0$. Thus, wing inertia can *enhance* the thrust of stiff wings and *reduce* the thrust of compliant wings, even so far as to produce drag.

It is interesting to consider how negative thrust relates to the retrograde motion observed by Spagnolie *et al.* (2010). To explore this possibility, we consider the case of a self-propelled wing driven at fixed frequency so that $KU^2 = 4\kappa/(\rho c^4 f^2)$ is constant. We set $R = 1$ as above and allow the swimming velocity to vary. In Fig. 6(b) we show the thrust coefficient against normalized velocity for five values of KU^2 . If KU^2 is small, due to either a compliant spring or a high driving frequency, the wing can generate negative thrust over a range of swimming speeds. Physically, negative thrust would slow the wing’s translation and - possibly in combination with nonlinear effects from finite amplitude or finite Reynolds number - could reverse the swimming direction. We find that wing com-

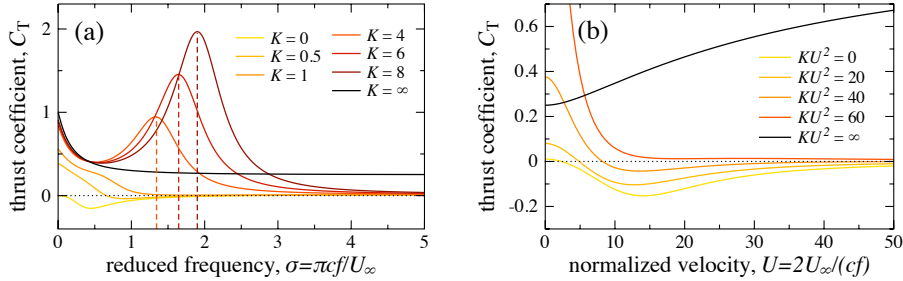


FIGURE 6. Effects of wing inertia. (a) Thrust coefficient versus reduced frequency for the same spring stiffnesses considered earlier, but with a wing/fluid inertia ratio of $R = 1$. The most compliant wings (yellow curves) can produce negative thrust. (b) Thrust coefficient versus translation velocity for freely swimming wings of different stiffnesses.

pliance and high driving frequency aid negative thrust production, which coincides with the conditions for which Spagnolie *et al.* (2010) observed retrograde motion. Importantly, since negative thrust does not occur for $R = 0$, our results suggest that some amount of wing inertia is essential for the retrograde effect.

6. Discussion

Through a new class of exact solutions, we have analyzed how compliance affects the propulsion of a wing flapping at small amplitude. Consistent with previous studies, we find dramatic performance improvements when the wing is driven near resonance and reduced performance when driven at higher frequencies. If the wing has sufficient inertia, it can even produce negative thrust. Having an analytical theory robust enough to capture these different behaviors, though somewhat surprising, offers a number of benefits. First, unlike experiments or simulations which must be run for a particular set of parameters, our solutions describe parameter space as a whole. This allows for quick estimates of important quantities, such as the resonant frequency or optimal thrust. Such estimates will likely be valuable even in situations that differ in detail, for example if the wing geometry or driving motion were different.

Another benefit is the precise derivation of the resonant frequency f_r , which is consistent with other estimates and measurements (see Masoud & Alexeev 2010; Dewey *et al.* 2013). Converting Eq. (3.4) to dimensional form gives the remarkably simple expression

$$2\pi f_r \sim \sqrt{\frac{\kappa}{I + I_a}} \quad \text{as } \kappa \rightarrow \infty. \quad (6.1)$$

Here, I is the wing's moment of inertia and $I_a = 9\pi\rho c^4/128$ is the added fluid inertia for a thin plate rotated about an endpoint (see Brennen 1982). This formula generalizes two well-understood cases: setting $I_a = 0$ recovers a torsional-spring-mass system flapping in a vacuum and setting $I = 0$ recovers a massless wing flapping in potential flow.

Of course, there are limitations to the applicability of a small-amplitude theory. At large enough driving amplitudes, nonlinear effects such as vortex-sheet roll up and leading-edge vortex shedding will bear their influence. These effects likely contribute to previously reported optimal behavior with respect to the Strouhal number fA/U_∞ (see Triantafyllou *et al.* 1993), which our theory cannot capture. Further, our solutions predict unbounded growth of the peak thrust coefficient with increasing K , whereas nonlinear effects would likely temper this growth as would be consistent with the scaling estimates of Dewey *et al.* (2013).

Finally, it is interesting that our solutions capture previously observed peaks in thrust but not in propulsive efficiency. Results in the literature vary regarding this trend: Heathcote & Gursul (2007) and Dewey *et al.* (2013) both observed efficiency peaks experimentally, while the simulations of Alben (2008) showed no such peaks. A common aspect of our study and Alben (2008) is that both use small-amplitude, inviscid theory, suggesting the efficiency optima to be a result of finite amplitude and/or viscosity. We point out that any type of fluid resistance, such as viscous drag, would dominate at low driving frequencies (since thrust vanishes like f^2), thus reducing $\eta = C_T/C_P$ and creating a peak at an intermediate frequency. In this way, efficiency optima might be explained as simply a viscous effect. Thus, while the resonant frequency depends only on inertia and wing stiffness, the frequency for optimal efficiency might be more sensitive to factors that influence the thrust-drag balance, such as the Reynolds number and wing geometry.

Acknowledgments

I would like to thank Silas Alben, Stephen Childress, Hassan Masoud, Sophie Ramanaarivo, Leif Ristroph, Michael Shelley, and Jun Zhang for helpful discussions. Also, I am indebted to an anonymous referee for pointing out the possible role of viscous resistance in creating an efficiency optimum.

Appendix A. Calculation of the fluid flow

We represent the dimensionless pressure, φ , as the real part of an analytic function $g(z, t) = \varphi + i\psi$. From Eq. (2.1), g is related to the complex velocity $w = u - iv$ by

$$\partial_z g = \partial_t w + U \partial_z w. \quad (\text{A } 1)$$

Evaluating on the wing surface and using Eq. (2.4) gives the boundary condition

$$\partial_x \psi = -(\partial_t + U \partial_x) v = -(\partial_t + U \partial_x)^2 h \quad \text{for } y \rightarrow \pm 0, -1 \leq x \leq 1. \quad (\text{A } 2)$$

The Kutta condition requires $|g| < \infty$ at the trailing edge $z = 1$, although a singularity is permitted at the leading edge $z = -1$. Additionally, g must decay at far field $|z| \rightarrow \infty$. The up-down symmetry of Eqs. (2.1)–(2.4) implies that v and ψ are even functions of y , and, by the Cauchy-Riemann equations, u and φ are odd functions of y . Our task is to solve Eqs. (A 1)–(A 2) subject to these boundary conditions and symmetry constraints.

Following Wu (1961), we conformally map the fluid domain surrounding the wing in the z -plane to the exterior of the unit disk in the ζ -plane via $z = (\zeta + 1/\zeta)/2$. On the perimeter of the disk, $\zeta = e^{i\xi}$, we have $x = \cos \xi$, giving $T_n(x) = \cos n\xi$ where T_n is the Chebyshev polynomial of degree n . We can therefore identify a Chebyshev series on the wing with a cosine series on the unit circle, from which Eqs. (2.3) and (2.4) imply

$$v = \left(\frac{1}{2} \lambda_0 + \lambda_1 \cos \xi \right) e^{2\pi j t} \quad \text{on the unit circle, } \zeta = e^{i\xi}, \quad (\text{A } 3)$$

$$\lambda_0 = 2\pi j \beta_0 + 2U \beta_1, \quad \lambda_1 = 2\pi j \beta_1. \quad (\text{A } 4)$$

The Kutta and far-field conditions imply g can be represented by the series given in Eq. (2.5), which is a combination of a pole at the leading edge and a multipole expansion about the origin. In that series, the coefficients a_n are real due to the symmetry in y . On

the unit circle $\zeta = e^{i\xi}$, φ and ψ inherit the expansions

$$\varphi = \left(\frac{1}{2}a_0 \tan \frac{\xi}{2} + \sum_{n=1}^{\infty} a_n \sin n\xi \right) e^{2\pi jt}, \quad (\text{A } 5)$$

$$\psi = \left(\frac{1}{2}a_0 + \sum_{n=1}^{\infty} a_n \cos n\xi \right) e^{2\pi jt}. \quad (\text{A } 6)$$

For $n \geq 1$, a_n is easily determined from Eqs. (A 2) and (A 6), which gives Eq. (2.7). To determine a_0 , one must invert Eq. (A 2) through time-dependent contour integration, resulting in Eq. (2.6).

To determine the fluid torque, \tilde{N}_f , we need the (dimensionless) pressure jump across the wing $[p] = \tilde{p}(x, 0^-, t) - \tilde{p}(x, 0^+, t)$, which can be determined from Eq. (A 5) as

$$[p] = \left(a_0 \sqrt{\frac{1-x}{1+x}} + 2a_1 \sqrt{1-x^2} + 4a_2 x \sqrt{1-x^2} \right) e^{2\pi jt}. \quad (\text{A } 7)$$

The fluid torque is then given by

$$\tilde{N}_f = \int_{-1}^1 [p] (x+1) dx = \frac{\pi}{2} (a_0 + 2a_1 + a_2) e^{2\pi jt}. \quad (\text{A } 8)$$

Appendix B. Calculation of thrust and power

We now calculate the forward thrust that the wing generates and the power required to drive it. We non-dimensionalize by the scales given in Section 2.1, so that force is scaled on $\rho c^3 f^2/8$ and power on $\rho c^4 f^3/16$. Dimensionless variables are indicated by tildes.

The thrust is decomposed as $\tilde{T} = \tilde{T}_p + \tilde{T}_s$, where \tilde{T}_p comes from the pressure difference across the wing and \tilde{T}_s is the leading-edge suction resulting from the flow singularity at $z = -1$. The first term is given by

$$\tilde{T}_p = \int_{-1}^1 [p]' \partial_x h' dx, \quad (\text{B } 1)$$

where prime indicates the real part with respect to j . The leading-edge suction can be calculated by contour integration as

$$\tilde{T}_s = \frac{\pi}{2U^2} ((a_0 e^{2\pi jt})')^2. \quad (\text{B } 2)$$

We then use Eqs. (2.3, 2.6, 2.7, A 7, B 1, B 2) to determine the time-averaged thrust,

$$\overline{\tilde{T}} = \frac{\pi}{4U^2} (a_0'^2 + a_0''^2) + \frac{\pi}{2} (a_0' \beta_1' + a_0'' \beta_1'') + \pi^3 (\beta_0' \beta_1' + \beta_0'' \beta_1''), \quad (\text{B } 3)$$

where the single and double primes denote real and imaginary parts in j respectively.

The power required to drive the wing is given by

$$\tilde{P} = - \int_{-1}^1 [p]' \partial_t h' dx \quad (\text{B } 4)$$

Using Eqs. (2.3, 2.6, 2.7, A 7, B 4) and taking the time average gives

$$\overline{\tilde{P}} = \frac{\pi^2}{2} (a_0'(\beta_0'' - \beta_1'') - a_0''(\beta_0' - \beta_1')) + 2\pi^3 U (\beta_0' \beta_1' + \beta_0'' \beta_1''). \quad (\text{B } 5)$$

To obtain the thrust and power coefficients defined in Eqs. (3.1) and (3.2), we simply rescale using $C_T = \overline{\tilde{T}}/(4\pi^3 \varepsilon^2)$ and $C_P = \overline{\tilde{P}}/(4\pi^3 U \varepsilon^2)$.

REFERENCES

- ALBEN, S. 2008 Optimal flexibility of a flapping appendage in an inviscid fluid. *J. Fluid Mech.* **614**, 355.
- ALBEN, S., WITT, C., BAKER, T. V., ANDERSON, E. & LAUDER, G. V. 2012 Dynamics of freely swimming flexible foils. *Phys. Fluids* **24** (5), 051901–051901.
- BERGOU, A. J., XU, S. & WANG, Z. 2007 Passive wing pitch reversal in insect flight. *J. Fluid Mech.* **591** (1), 321–337.
- BRENNEN, C. E. 1982 A review of added mass and fluid inertial forces. *Tech Rep.* CR 82.010. Contract no. N62583-81-MR-554. Naval Civil Engineering Laboratory.
- DAI, H., LUO, H. & DOYLE, J. F. 2012 Dynamic pitching of an elastic rectangular wing in hovering motion. *J. Fluid Mech.* **693**, 473–499.
- DEWEY, P. A., BOSCHITSCH, B. M., MOORED, K. W., STONE, H. A. & SMITS, A. J. 2013 Scaling laws for the thrust production of flexible pitching panels. *J. Fluid Mech.* **732**, 29–46.
- ENNOS, A. R. 1988 The importance of torsion in the design of insect wings. *J. Exp. Biol.* **140** (1), 137–160.
- FISH, F. E. 1993 Power output and propulsive efficiency of swimming bottlenose dolphins (*tursiops truncatus*). *J. Exp. Biol.* **185** (1), 179–193.
- HEATHCOTE, S. & GURSUL, I. 2007 Flexible flapping airfoil propulsion at low reynolds numbers. *AIAA J.* **45** (5), 1066–1079.
- KANG, C. K., AONO, H., CESNIK, C. E. S. & SHYY, W. 2011 Effects of flexibility on the aerodynamic performance of flapping wings. *J. Fluid Mech.* **689** (1), 32–74.
- KATZ, J. & WEIHS, D. 1978 Hydrodynamic propulsion by large amplitude oscillation of an airfoil with chordwise flexibility. *J. Fluid Mech.* **88** (03), 485–497.
- LUCAS, K. N., JOHNSON, N., BEAULIEU, W. T., CATHCART, E., TIRRELL, G., COLIN, S. P., GEMMELL, B. J., DABIRI, J. O. & COSTELLO, J. H. 2014 Bending rules for animal propulsion. *Nature communications* **5**.
- MASOUD, H. & ALEXEEV, A. 2010 Resonance of flexible flapping wings at low reynolds number. *Phys. Rev. E* **81** (5), 056304.
- MICHELIN, S. & SMITH, S. G. L. 2009 Resonance and propulsion performance of a heaving flexible wing. *Phys. Fluids* **21**, 071902.
- RAMANANARIVO, S., GODOY-DIANA, R. & THIRIA, B. 2011 Rather than resonance, flapping wing flyers may play on aerodynamics to improve performance. *P. Natl. Acad. Sci. USA* **108** (15), 5964–5969.
- RISTROPH, L. & CHILDRESS, S. 2014 Stable hovering of a jellyfish-like flying machine. *J. R. Soc. Interface* **11** (92), 20130992.
- ROZHDESTVENSKY, K. V. & RYZHOV, V. A. 2003 Aerohydrodynamics of flapping-wing propulsors. *Prog. Aerosp. Sci.* **39** (8), 585–633.
- SHANG, J. K., COMBES, S. A., FINIO, B. M. & WOOD, R. J. 2009 Artificial insect wings of diverse morphology for flapping-wing micro air vehicles. *Bioinspir. Biomim.* **4** (3), 036002.
- SPAGNOLIE, S. E., MORET, L., SHELLEY, M. J. & ZHANG, J. 2010 Surprising behaviors in flapping locomotion with passive pitching. *Phys. Fluids* **22** (4), 041903–041903.
- THIRIA, B. & GODOY-DIANA, R. 2010 How wing compliance drives the efficiency of self-propelled flapping flyers. *Phys. Rev. E* **82** (1), 015303.
- TRIANTAFYLLOU, G. S., TRIANTAFYLLOU, M. S. & GROSENBAUGH, M. A. 1993 Optimal thrust development in oscillating foils with application to fish propulsion. *J. Fluids Struct.* **7** (2), 205–224.
- VANDENBERGHE, N., CHILDRESS, S. & ZHANG, J. 2006 On unidirectional flight of a free flapping wing. *Phys. Fluids* **18** (1), 014102–014102.
- VOGEL, S. 1994 *Life in moving fluids: the physical biology of flow*. Princeton University Press.
- WU, T. Y. 1961 Swimming of a waving plate. *J. Fluid Mech.* **10** (03), 321–344.
- WU, T. Y. 2011 Fish swimming and bird/insect flight. *Annu. Rev. Fluid Mech.* **43**, 25–58.
- YOUNG, J., WALKER, S. M., BOMPHELY, R. J., TAYLOR, G. K. & THOMAS, A. L. R. 2009 Details of insect wing design and deformation enhance aerodynamic function and flight efficiency. *Science* **325** (5947), 1549–1552.